SPIN90 associates with mDia1 and the Arp2/3 complex to regulate cortical actin organization

Luyan Cao, Amina Yonis, Malti Vaghela, Elias H Barriga, Priyamvada Chugh, Matthew B Smith, Julien Maufront, Geneviève Lavoie, Antoine Méant, Emma Ferber, et al.

▶ **To cite this version:**

Luyan Cao, Amina Yonis, Malti Vaghela, Elias H Barriga, Priyamvada Chugh, et al.. SPIN90 associates with mDia1 and the Arp2/3 complex to regulate cortical actin organization. Nature Cell Biology, 2020, 22, pp.803 - 814. ⟨10.1038/s41556-020-0531-y⟩. ⟨hal-03006846⟩

HAL Id: hal-03006846

https://hal.science/hal-03006846v1

Submitted on 19 Jan 2021

HAL is a multi-disciplinary open access archive for the deposit and dissemination of scientific research documents, whether they are published or not. The documents may come from teaching and research institutions in France or abroad, or from public or private research centers.

L'archive ouverte pluridisciplinaire **HAL**, est destinée au dépôt et à la diffusion de documents scientifiques de niveau recherche, publiés ou non, émanant des établissements d'enseignement et de recherche français ou étrangers, des laboratoires publics ou privés.

HAL Authorization

SPIN90 associates with mDia1 and the Arp2/3 complex to regulate cortical actin organisation

Luyan Cao[1]*, Amina Yonis[2,3]*, Malti Vaghela[2,4]*, Elias H Barriga[3,12], Priyamvada Chugh[5], Matthew B Smith[5,13], Julien Maufront[6,7], Geneviève Lavoie[8], Antoine Méant[8], Emma Ferber[2], Miia Bovellan[2,3], Art Alberts[9,†], Aurélie Bertin[6,7], Roberto Mayor[3], Ewa K. Paluch[5,10,14], Philippe P. Roux[8,11], Antoine Jégou[1,#], Guillaume Romet-Lemonne[1,#], Guillaume Charras[2,3,10,#]

1. Université de Paris, CNRS, Institut Jacques Monod, 75013 Paris, France
2. London Centre for Nanotechnology, University College London, WC1H 0AH, UK
3. Department of Cell and Developmental Biology, University College London, WC1E 6BT, UK
4. Department of Physics and Astronomy, University College London, WC1E 6BT, UK
5. MRC-Laboratory for Molecular Cell Biology, University College London, WC1E 6BT, UK
6. Laboratoire Physico Chimie Curie, Institut Curie, PSL Research University, CNRS UMR168, 75005 Paris, France
7. Sorbonne Universités, 75005 Paris, France
8. Institute for Research in Immunology and Cancer, Université de Montréal, Montréal, Canada
9. Van Andel research institute, Grand Rapids, MI, USA
10. Institute for the Physics of Living Systems, University College London, WC1E 6BT, UK
11. Department of Pathology and Cell Biology, Université de Montréal, Montréal, Canada

Present addresses:

12. Instituto Gulbenkian de Ciência, 2780-156 Oeiras, Portugal.
13. The Francis-Crick institute, London, UK
14. Physiology, Development and Neuroscience, University of Cambridge, Cambridge, UK

† Deceased

*Equal contribution

#Equal contribution

Authors for correspondence: Guillaume Charras (g.charras@ucl.ac.uk), Guillaume Romet-Lemonne (romet@ijm.fr) and Antoine Jégou (antoine.jegou@ijm.fr).

Lead contact: Guillaume Charras

Summary

Cellular shape is controlled by the submembranous cortex, an actomyosin network mainly generated by two actin nucleators: the Arp2/3 complex and the formin mDia1. Changes in relative nucleator activity may alter cortical organization, mechanics and cell shape. Here, we investigate how nucleation-promoting factors (NPFs) mediate interaction between nucleators. In vitro, the NPF SPIN90 promotes formation of unbranched filaments by Arp2/3, a process thought to provide the initial filament for generation of dendritic networks. Paradoxically, in cells, SPIN90 appears to favour a formin-dominated cortex. Our experiments *in vitro* reveal this feature stems mainly from two mechanisms: efficient recruitment of mDia1 to SPIN90-Arp2/3 nucleated filaments and formation of a ternary SPIN90-Arp2/3-mDia1 complex that greatly enhances filament nucleation. Both mechanisms yield rapidly elongating filaments with mDia1 at their barbed ends and SPIN90-Arp2/3 at their pointed ends. Thus, in networks, SPIN90 lowers branching densities and increases the proportion of long filaments elongated by mDia1.

Introduction

One of the most striking properties of living cells is their ability to change shape during physiological processes, such as division, migration, and differentiation. Shape changes are governed by mechanical changes in the cortex, a thin network of actomyosin below the membrane[1]. Changes in cortical mechanics can originate from changes in myosin activity[2] or cortex architecture, which arise from changes in actin filament length[3] or network organization[4]. One potential mechanism to control cortex architecture involves regulation of actin nucleators. Indeed, *in vitro,* in the presence of profilin, formins generate longer filaments than those created by Arp2/3-mediated branching[5,6] and, in cells, single molecule experiments suggest a similar trend[7]. Furthermore, actin nucleators generate varied network topologies ranging from highly branched networks generated by the Arp2/3 complex to linear arrays generated by formins and Ena/VASP. Thus, a switch in the dominant F-actin nucleator might also alter network organization. However, little is known about how nucleator activity is controlled to change network topology and mechanics.

Many cellular actin-based structures such as the cortex, the leading edge of migrating cells, phagocytic cups, and intercellular junctions require both formins and the Arp2/3 complex for their formation[8-12]. This is surprising because the actin networks they generate differ extensively in their topology, protein interactors, dynamics, and force generation[4,11,13,14]. Some reports have shown synergistic action of pointed end nucleators (such as Spire or APC) with barbed end nucleators (such as formins)[15-17], whereas others have shown sequential action of nucleators[18]. Overall, these observations underscore the importance of nucleator crosstalk for the generation of functionally optimal actin structures in cells.

In addition to RhoGTPases, Nucleation Promoting Factors (NPFs) are involved in activating nucleators or maintaining their activity[19]. Arguably, the best studied NPF is the Wave regulatory complex (WRC), which consists of five subunits (SRA1, NAP1, Abi1, BRK1, WAVE2) and activates the Arp2/3 complex to generate branched actin networks[19]. After the Wave complex detaches from Arp2/3, another NPF, cortactin, protects Arp2/3 against debranching[19]. Some NPFs can interact with multiple nucleators, making them prime candidates to mediate interplay. IQGAP1 can maintain the activity of mDia1 via its C-terminal DBR domain (**Fig 1A**) but also promote Arp2/3 activity by interacting with N-WASp and the Wave complex via its N-terminal Calponin Homology Domain (CHD)[20-22]. Another NPF, SPIN90/DIP/WISH/NCKIPSD, has been reported to interact with Arp2/3 in some studies and formins in others. SPIN90 forms a complex with Arp2/3 to stimulate formation of unbranched filaments[23]. In addition to providing the initial filament necessary for generation of dendritic networks by the WRC and Arp2/3[24], very recent work proposes that SPIN90 competes with the WRC to modulate the degree of branching in networks[25]. Furthermore, SPIN90 can interact with the diaphanous related formins (DRF) mDia1 and mDia2 via its LRR and/or SH3 domains (**Fig 1A**)[26,27] and, surprisingly, it inhibits actin filament elongation by mDia2 but not mDia1[26].

Here, we examine how NPFs regulate nucleator activity in the actin cortex to control its organization, assembly kinetics, and mechanics. We show that IQGAP1 controls the activity of the formin mDia1, WRC regulates Arp2/3 branching activity, and SPIN90 mediates an unexpected synergistic action between Arp2/3 and mDia1.

Results

Several NPFs localise to the actin cortex

Previous proteomic analyses revealed the presence of two actin nucleators in the cortex of M2 blebbing melanoma cells, the Arp2/3 complex and the formin mDia1[9]. Several NPFs that could regulate these nucleators were also present (**Supplementary Table 1**): the Wave Regulatory Complex, IQGAP1, cortactin, SPIN90, and Fli-1 (protein flightless-I homolog, an NPF that prevents formin autoinhibition[28]). Published proteomic datasets indicate that these NPFs are also expressed in HeLa cells (**Supplementary Table 2**), suggesting they may play a general role in controlling cortical nucleator activity[29-31].

We examined NPF localization in M2 melanoma cell blebs and metaphase HeLa cells. Blebs provide a snapshot into the cortex life cycle[32], while mitosis represents a key physiological function of the cortex. All NPFs identified in proteomics localized to the cortex of mitotic HeLa cells and retracting blebs, where a cortex reforms *de novo* by nucleation[9] (**Fig 1B,C** and **Extended Data Fig. 1A-D**). Thus, these NPFs are promising candidates for controlling the activity of cortical nucleators.

We concentrated on WRC and SPIN90 because they mediate the transition from branched to unbranched actin networks nucleated by Arp2/3, and IQGAP1 and SPIN90 because they may coordinate the activity of Arp2/3 and mDia1.

SPIN90 depletion mimics mDia1 depletion in blebbing cells

To determine how NPFs modulate nucleator activity, we examined their effect on bleb size in M2 cells knowing that Arp2/3 depletion results in small blebs, whereas mDia1 depletion results in large blebs[9]. As expected, IQGAP1 depletion resulted in more cells with large blebs (**Fig 1D, Supplementary Figure 1H, J**), consistent with a role in maintaining mDia1 activity[20], and depletion of WRC subunits resulted in small blebs (**Fig 1E-F; Supplementary Figure 1H,K-L**), consistent with its known role in regulating Arp2/3. Surprisingly, SPIN90 depletion resulted in large blebs (**Fig 1D,F; Supplementary Figure 1H-I**), suggesting that SPIN90 cooperates with mDia1 directly or indirectly rather than inhibiting DRF formins as previously reported[26]. These unexpected results (summarised in **Supplementary Table 3**) led us to focus on SPIN90.

SPIN90 depletion perturbs cell proliferation

Previous work showed that mDia1 depletion increased cell death, whereas Arp2/3 depletion did not[9]. When we examined how NPF depletion affected proliferation in HeLa cells, we found that depletion of WRC subunits did not increase cell death, similar to Arp2/3 depletion, but IQGAP1 depletion led to a two-fold increase in cell death (**Fig 1G-H, Supplementary Figure 1A-G**). This latter effect was likely mediated by interaction with mDia1 because expression of the mouse IQGAP1 DBR domain in IQGAP1-depleted cells decreased cell death to near baseline levels (**Fig 1A,I**). Like mDia1 depletion, SPIN90 depletion increased cell death three-fold (**Fig 1H, Supplementary Figure 1A-G**). We confirmed the specificity of depletion by expressing full-length mouse SPIN90 in SPIN90-depleted cells (**Fig 1I**). Examination of changes in mRNA transcript abundance by qPCR confirmed that the effect of SPIN90 and IQGAP1 depletion was not due to indirect regulation of NPFs or nucleators at the transcriptional level (**Supplementary Figure 2**). Thus, mDia1 activity regulated by IQGAP1 and SPIN90 is necessary for proliferation (**Supplementary Table 3**).

SPIN90 depletion decreases cortical mesh size in blebs

We then examined how NPF depletion affects the organization of F-actin in the cortex of M2 cell blebs. Previous work showed that depletion of mDia1 led to large gaps within the cortex, while Arp2/3 depletion led to no clear change in actin filament density[9]. IQGAP1 depletion led to a two-fold increase

in the proportion of gaps with diameters larger than 140nm (**Fig 2A-B, Supplementary Figure 3**), similar to mDia1 depletion. NAP1 depletion did not significantly change gap diameter distribution, as ACTR2 depletion (**Fig 2A,B, Supplementary Figure 3**). SPIN90 depletion led to a visibly denser cortex (**Fig 2A**) and a 20% increase in the proportion of gaps less than 30nm in diameter (**Fig 2B, Supplementary Figure 3**). This was surprising because previous cell-scale assays showed that SPIN90 depletion phenocopied mDia1 depletion (**Fig 1**). However, SPIN90 has been proposed to compete with WRC for Arp2/3 to regulate the degree of branching[25]. Depletion of SPIN90 might therefore lead to a denser cortical network because of increased branching. Thus, SPIN90 may mediate crosstalk between mDia1 and Arp2/3 (**Supplementary Table 3**).

SPIN90 governs cortical actin density and thickness in mitotic cells

We next determined if NPF depletion affected cortical thickness and density during mitosis in HeLa cells by analyzing the fluorescence profile of an F-actin fluorescent reporter with respect to the plasma membrane (**Fig 2C**)[33]. Previous work showed that depletion of mDia1 leads to a decrease in cortical thickness whereas depletion of Arp2/3 does not affect thickness[3]. Depletion of IQGAP1 and NAP1 had no impact on cortical thickness or density (**Fig 2D, 2E**). Similar to mDia1 depletion[3], SPIN90 depletion significantly decreased cortical thickness by ~25% (**Fig 2D**). However, SPIN90 depletion also led to a ~50% increase in cortex density (**Fig 2E**), something not observed with mDia1 depletion[3] but consistent with the smaller cortical gap sizes measured by SEM (**Fig 2A-B**).

SPIN90 controls cortical actin accumulation rate in mitotic cells

To quantitatively examine the role of NPFs in regulating nucleator activity, we measured the cortical F-actin accumulation rate in blebs generated by ablation of the cortex of a metaphase HeLa cell using a pulsed UV laser[34] (**Fig 3A, Extended Data Fig. 2).** Previous work showed that mDia1 depletion decreases F-actin accumulation rate, whereas depletion of Arp2/3 subunits increases it[9]. Depletion of IQGAP1 and NAP1 mirrored the respective effects of mDia1 and Arp2/3 depletion, consistent with their proposed roles (**Fig 3C-D**). SPIN90 depletion led to a significant decrease in actin regrowth rate, again arguing for cooperation with mDia1 (**Fig 3B,D**). Together these results indicate that NPFs regulate actin network growth kinetics in the mitotic cortex (**Supplementary Table 3**).

SPIN90 depletion stiffens the mitotic cortex

Recent work has shown that modulating nucleator activity affects cell mechanics[2,3,7]. To probe cortical mechanics, we indented rounded metaphase HeLa cells with a blunt AFM tip limiting ourselves to depths of <500nm, where the cortex dominates mechanics[35] (**Fig 3E**). The apparent stiffness measured is sensitive to contributions from cortical elasticity and tension.

Inhibition of formins with SMIFH2 led to a significant decrease in apparent stiffness, consistent with previous results[7] (**Fig 3G)**. However, mDia1 depletion had no effect (**Fig 3G**), perhaps because of a more acute effect of SMIFH2 or a low sensitivity of apparent stiffness to reduction in cortical tension[3]. Inhibition of the Arp2/3 complex with CK666 or depletion with shRNA led to a greater than two-fold significant increase in apparent stiffness that could be reversed by blebbistatin treatment (**Fig 3F**, **Extended Data Fig. 2E**), consistent with observations that Arp2/3 complex inhibition increases cell contractility[36].

Depletion of NAP1 led to a ~two-fold increase in apparent stiffness, consistent with Arp2/3 depletion (**Fig 3F**) but in contradiction with reports of a decrease in tension for SRA1 depletion[37]. Depletion of IQGAP1 did not change apparent stiffness, similar to mDia1, but surprisingly, SPIN90 depletion led to a ~two-fold increase (**Fig 3G**). Changes in apparent stiffness did not correlate with changes in cortical pMLC abundance (**Extended Data Fig. 3, Supplementary Table 3**) or cortical density (**Fig 2E**), suggesting that they stem from complex changes in network organization at the microscale.

SPIN90 is essential for cell division during embryonic morphogenesis

Having shown an unexpected role for SPIN90 in cancer cells, we examined its role in embryonic tissues where cells must frequently divide and change shape for tissue morphogenesis. Previous work has shown roles for the WRC and IQGAP1 during embryonic morphogenesis[38,39] as well as the presence of mDia1 in the gastrula epithelium[40]. We therefore investigated a role for the SPIN90 ortholog in early *Xenopus Laevis* embryos using morpholino injections (**Supplementary Figure 4, Supplementary Figure 5**).

SPIN90-depleted embryos initially developed normally but, by stage 9, they displayed epidermal cells many fold larger than in controls because they were multinucleated (**Fig 4A-B**), consistent with the role for SPIN90 in cell cycle progression observed in cancer cells (**Fig 1H,I**). This phenotype eventually led to epidermis rupture and embryonic death at gastrulation. The late phenotype onset is perhaps due to reliance on maternal protein prior to mid-blastula transition or to a change in the nucleation pathway for cortical actin after ectoderm specification around stage 7 [41]. Cell enlargement and multi-nucleation could both be rescued by co-injection of full-length mouse SPIN90 (**Fig 4C-D**). Junctional F-actin in SPIN90-depleted embryos at stage 9 appeared separated from the cell membrane (arrows, **Fig 4E**), a phenotype also rescued by co-injection of full-length mouse SPIN90. Thus, SPIN90 is necessary for embryonic morphogenesis likely through a role in cell division.

SPIN90 mediates crosstalk between nucleators to control network organization

Thus far, our data indicate that IQGAP1 acts as an NPF for mDia1 and that the WRC acts as an NPF for the Arp2/3 complex (**Supplementary Table 3**). Many of the phenotypes linked to SPIN90 depletion suggest that it acts cooperatively with mDia1 (bleb size, cell cycle progression, thickness, actin accumulation rate) and stiffness measurements suggest it acts as an NPF for Arp2/3, while it presents a distinct phenotype in other assays (mesh size, cortical density) (**Supplementary Table 3**). As SPIN90 can interact with both nucleators, we examined a role in mediating their crosstalk using purified proteins.

After confirming that SPIN90 interacts with each nucleator separately, without enhancing mDia1 activity (**Extended Data Fig. 4, Supplementary Figure 6**), we examined how SPIN90 altered the organization of F-actin networks in a minimal system of purified proteins containing actin, profilin, Arp2/3, VCA (a domain of Wave-2 that activates Arp2/3) and mDia1. In the absence of SPIN90, nucleation of mother filaments was slow, generating a network consisting of few very densely branched regions (**Fig 5A**). When SPIN90 was present, filaments were rapidly nucleated giving rise to a more homogenous network with longer filaments. SPIN90 greatly increased the nucleation of mother filaments and decreased the density of branches on mother filaments (**Fig 5B-E, Supplementary Figure 7**), consistent with recent results[25]. Overall, adding SPIN90 leads to the formation of more barbed ends, which appear more evenly distributed over the surface (**Fig 5A-C**). Strikingly, the fraction of mDia1-bearing barbed ends (identified by their rapid elongation in the presence of profilin) also grew with increasing concentrations of SPIN90 (**Fig 5F**), suggesting that SPIN90 somehow favors the recruitment of mDia1 to barbed ends.

Thus, SPIN90 modulates network organization by shifting the balance of branched to unbranched filaments generated by the Arp2/3 complex and by facilitating the addition of mDia1 to barbed ends to generate long filaments. Importantly, these effects were noticeable at NPF ratios close to those present in cells (**Supplementary Table 2**).

Filaments nucleated by SPIN90-Arp2/3 efficiently recruit mDia1

Next, we investigated if mDia1 might have different propensities to bind barbed ends generated with and without SPIN90 (**Extended Data Fig. 5**, **Supplementary Results**, **Supplementary Figure 8**). We found that mDia1 was equally recruited by the barbed ends of mother filaments and branches in dendritic networks nucleated by Arp2/3 and Wave (**Extended Data Fig. 5A**). Intriguingly, when mDia1 was added to a mix of preformed filaments nucleated either spontaneously or by SPIN90-Arp2/3, we found the latter recruited mDia1 more efficiently to their barbed ends (**Extended Data Fig. 5B**). Further experiments using microfluidics revealed that mDia1 was recruited 2-fold faster to barbed ends nucleated by SPIN90-Arp2/3 than to those nucleated by spectrin-actin seeds (**Figure 6A, Extended Data Fig. 9A-B**). Finally, we found that recruitment of mDia1 to SPIN90-Arp2/3 nucleated filaments was further enhanced when mDia1 was present during nucleation (**Extended Data Fig. 5C, Supplementary Figure 8A**). Together, these data suggested that SPIN90-Arp2/3 may recruit mDia1 to nucleate a rapidly growing filament.

SPIN90 forms a ternary complex with Arp2/3 and mDia1 to nucleate fast growing filaments

To probe the existence of a ternary complex, we performed pull-down experiments that showed that mDia1 binds to the SPIN90-Arp2/3 complex with a higher affinity than to SPIN90 alone and that the SH3 domain of SPIN90 is not necessary for mDia1 to bind the SPIN90-Arp2/3 complex (**Extended Data Fig. 6A**, **Supplementary Results, Supplementary Figure 8C**). Next, we performed negative staining electron microscopy experiments using mixtures of Arp2/3 with and without SPIN90 and mDia1 (**Fig 6B, Extended Data Fig. 7-8**). When mDia1 was added to the Arp2/3 complex, 3D reconstructions of Arp2/3 could be docked with published structures[42] with no additional electron density. When SPIN90 was added to the Arp2/3 complex, an additional electron density was present in the region where SPIN90 has been shown to interact with Arp2/3 [43]. Finally, when both SPIN90 and mDia1 were included, a further electron density that could be docked with a dimer of FH2 was present close to the Arp2 and Arp3 subunits (**Fig 6B**). These results confirm the formation of a ternary SPIN90-Arp2/3-mDia1 complex, and suggest that mDia1 may interact with the Arp2/3 complex rather than SPIN90 in the ternary complex.

To characterize filament nucleation by the ternary SPIN90-Arp2/3-mDia1 complex, we used a microfluidics assay in which we exposed a SPIN90-decorated surface sequentially to Arp2/3 followed by mDia1, before flowing in profilin-actin to enable filament nucleation and growth (**Fig 6C-E**). We observed three populations of filaments: (*i*) slow growing filaments, (*ii*) filaments that elongated slowly and suddenly switched to rapid elongation, and (*iii*) filaments elongating rapidly from the start. Since rapid elongation indicates the presence of mDia1 at the barbed end[44], we interpreted population (iii) as being nucleated by the ternary complex.

The nucleation rate of population (i) was identical to that of the filaments in a region of the same microchamber which we did not expose to mDia1 (**Fig 6E**, **Extended Data Fig. 9C**), and to that measured in an independent experiment with no mDia1 (**Extended Data Fig. 4A**) indicating that population (i) corresponds to filaments nucleated by SPIN90-Arp2/3 that did not bind mDia1. The nucleation rate of population (ii) was comparable to population (i). We thus hypothesized that these slow-then-fast growing filaments were also nucleated by SPIN90-Arp2/3 and later captured an mDia1 adsorbed on the surface. Control experiments (**Extended Data Fig. 6B**) indicated that such events could indeed account for a significant fraction of population (ii). The filaments in population (iii) were nucleated 5-fold faster than the filaments nucleated by SPIN90-Arp2/3 (**Fig 6E**), consistent with the notion that they are nucleated by the ternary SPIN90-Arp2/3-mDia1 complex. The aforementioned control experiment (**Extended Data Fig. 6B**) also confirmed that population (iii) does not result from the capture of mDia1 after nucleation. Together, our results indicate that the ternary SPIN90-Arp2/3-

mDia1 complex is a much more potent nucleator than SPIN90-Arp2/3, and that the resulting filaments have SPIN90-Arp2/3 bound to their pointed end and mDia1 bound to their barbed end.

To directly observe nucleation of filaments by this ternary complex, we performed single molecule experiments using fluorescently labelled mDia1 and SPIN90. When mixing these proteins with Arp2/3, profilin and actin (15% Alexa488 labelled), we observed rapidly growing filaments bearing mDia1 at their barbed end. Even though labelled SPIN90 was less active than unlabelled SPIN90, it was present at the pointed end of these rapidly growing filaments (**Fig 7A**). This observation illustrates that, as in the absence of mDia1 (**Extended Data Fig. 4A**), SPIN90 and Arp2/3 remain at the pointed end of filaments after nucleation (**Fig 6C-E**). Filament nucleation was challenging to observe but, colocalization of SPIN90 with mDia1 could sometimes be observed prior to the appearance of fluorescently-labelled actin, which then separated the peaks of SPIN90 and mDia1 fluorescence, as expected since each protein occupies a different end of the growing filament (**Fig 7B**).

Overall, our *in vitro* observations show that SPIN90 activates Arp2/3 to nucleate linear filaments at the expense of Arp2/3 branching, and that these filaments have an enhanced likelihood of bearing mDia1 at their barbed ends thanks to (at least) two key features: the efficient recruitment of mDia1 to SPIN90-Arp2/3 nucleated filaments and the formation of a ternary SPIN90-Arp2/3-mDia1 complex that greatly enhances filament nucleation. Both mechanisms result in rapidly elongating filaments with mDia1 at their barbed ends and SPIN90-Arp2/3 at their pointed ends (**Fig 7C**).

Discussion

We identify an NPF, SPIN90, that synergizes the action of Arp2/3 and mDia1 by forming a ternary complex and has wide-ranging effects in governing actin network architecture.

The organization of F-actin networks is central to specifying their physiological function and mechanics. Understanding what mediates the passage from one network organization to another is a key unresolved question in cell biology. Competition between nucleators can help specify structures. Indeed, the passage from the two dimensional branched network topologies found in lamellipodia to the one dimensional topologies present in filopodia appears mediated by competition between actin nucleators for G-actin monomers, regulated by profilin[45,46]. We report here that SPIN90, which thus far had only been considered as a mechanism to nucleate the mother filaments for the formation of branched networks and as a means to modulate branching density ([23,25], **Fig 5**), is actually a potent enhancer of formin mDia1. SPIN90 competes with the WRC to tune the degree of Arp2/3-branching and co-opts formins to generate long rapidly-growing filaments to generate a rich variety of actin filament networks (**Supplementary Figure 13**). Importantly, such transitions were observed for ratios of SPIN90 to WRC close to those present in cells (**Supplementary Table 2**). Overall, our data indicate that SPIN90 regulates branching, filament growth rate and the resulting filament length, which are key parameters of the network's architecture (**Supplementary Figure 13**).

Our data reveal that SPIN90 allows synergistic action between mDia1 and Arp2/3 through at least two mechanisms, both resulting in increased nucleation of fast-growing actin filaments with SPIN90-Arp2/3 at their pointed ends and mDia1 at their barbed ends (**Fig 7C**).

First, mDia1 displays an enhanced apparent on-rate for the barbed ends of filaments generated by SPIN90-Arp2/3. This surprising observation may either result from microstructural differences in the barbed ends induced at nucleation[13] or from recruitment of mDia1 to the pointed end by binding to SPIN90-Arp2/3 followed by diffusion of mDia1 along the filament towards the barbed end, as already reported for mDia1 in a different context[47].

Second, we showed that SPIN90-Arp2/3 can form a ternary complex with mDia1 that increases filament nucleation five-fold compared to SPIN90-Arp2/3 alone. Our EM data (**Fig 6B**) and single filament observations (**Fig 6C-E**) suggest that, following activation of Arp2/3 by SPIN90, a dimer of the FH2 domain of mDia1 binds to Arp2 and Arp3, which mimic a barbed end, to enhance nucleation and catalyse addition of monomers to the new filament. Such a "rocket launching" complex has been described for collaborative action of Adenomatous polyposis coli (APC) and mDia1[48] but not for Arp2/3 and mDia1, arguably the two most abundant actin nucleators. After elongation starts, our in vitro data indicate that mDia1 remains associated with the barbed end of the filament, whereas SPIN90-Arp2/3 remains at the pointed end (**Fig 6C-E, 7A-B**) (as already reported in the absence of mDia1[24]). This formation mechanism takes advantage of the efficient nucleation activity of the Arp2/3 complex and rapid filament elongation by mDia1.

The total amounts of SPIN90 and other NPFs in cells can be estimated based on proteomics data and measurements of cellular actin concentration[31,49] (**Supplementary Table 2**). While determining the concentrations of available, active proteins in the cortical region is more challenging (e.g., the WRC and mDia1 need to be activated and are likely bound to the membrane), we can estimate the relevant SPIN90 concentration to be in the 50-200 nM range (**Supplementary Table 2**).

In addition, in cells, our data indicate that IQGAP1 also modulates mDia1 activity (**Figs 1-3**). IQGAP1 may bind active mDia1 following release from the ternary complex (**Fig 7C**), allowing to maintain elongation activity through its C-terminal DBR domain (**Fig 1A**) and perhaps to scaffold mDia1 to the cortex through its N-terminal CHD domains.

Overall, our data show that the activity of the two main cortical actin nucleators, mDia1 and Arp2/3, is modulated by the interplay of three NPFs to finely tune cortical actin organization, kinetics, and mechanics.

References

1 Salbreux, G., Charras, G. & Paluch, E. Actin cortex mechanics and cellular morphogenesis. *Trends in Cell Biology* **22**, 536-545, doi:http://dx.doi.org/10.1016/j.tcb.2012.07.001 (2012).

2 Ramanathan, S. P. *et al.* Cdk1-dependent mitotic enrichment of cortical myosin II promotes cell rounding against confinement. *Nat Cell Biol* **17**, 148-159, doi:10.1038/ncb3098 (2015).

3 Chugh, P. *et al.* Actin cortex architecture regulates cell surface tension. *Nat Cell Biol* **19**, 689-697, doi:10.1038/ncb3525 (2017).

4 Ennomani, H. *et al.* Architecture and Connectivity Govern Actin Network Contractility. *Curr Biol* **26**, 616-626, doi:10.1016/j.cub.2015.12.069 (2016).

5 Kovar, D. R. & Pollard, T. D. Progressing actin: Formin as a processive elongation machine. *Nat Cell Biol* **6**, 1158-1159, doi:10.1038/ncb1204-1158 (2004).

6 Romero, S. *et al.* Formin is a processive motor that requires profilin to accelerate actin assembly and associated ATP hydrolysis. *Cell* **119**, 419-429, doi:10.1016/j.cell.2004.09.039 (2004).

7 Fritzsche, M., Erlenkamper, C., Moeendarbary, E., Charras, G. & Kruse, K. Actin kinetics shapes cortical network structure and mechanics. *Sci Adv* **2**, e1501337, doi:10.1126/sciadv.1501337 (2016).

8 Acharya, B. R. *et al.* Mammalian Diaphanous 1 Mediates a Pathway for E-cadherin to Stabilize Epithelial Barriers through Junctional Contractility. *Cell Rep* **18**, 2854-2867, doi:10.1016/j.celrep.2017.02.078 (2017).

9 Bovellan, M. *et al.* Cellular control of cortical actin nucleation. *Curr Biol* **24**, 1628-1635, doi:10.1016/j.cub.2014.05.069 (2014).

10 May, R. C., Caron, E., Hall, A. & Machesky, L. M. Involvement of the Arp2/3 complex in phagocytosis mediated by FcgammaR or CR3. *Nat Cell Biol* **2**, 246-248, doi:10.1038/35008673 (2000).

11 Ridley, A. J. Life at the leading edge. *Cell* **145**, 1012-1022, doi:10.1016/j.cell.2011.06.010 (2011).

12 Seth, A., Otomo, C. & Rosen, M. K. Autoinhibition regulates cellular localization and actin assembly activity of the diaphanous-related formins FRLalpha and mDia1. *J Cell Biol* **174**, 701-713, doi:10.1083/jcb.200605006 (2006).

13 Michelot, A. & Drubin, D. G. Building distinct actin filament networks in a common cytoplasm. *Curr Biol* **21**, R560-569, doi:10.1016/j.cub.2011.06.019 (2011).

14 Murrell, M., Oakes, P. W., Lenz, M. & Gardel, M. L. Forcing cells into shape: the mechanics of actomyosin contractility. *Nat Rev Mol Cell Biol* **16**, 486-498, doi:10.1038/nrm4012 (2015).

15 Okada, K. *et al.* Adenomatous polyposis coli protein nucleates actin assembly and synergizes with the formin mDia1. *J Cell Biol* **189**, 1087-1096, doi:10.1083/jcb.201001016 (2010).

16 Quinlan, M. E., Hilgert, S., Bedrossian, A., Mullins, R. D. & Kerkhoff, E. Regulatory interactions between two actin nucleators, Spire and Cappuccino. *J Cell Biol* **179**, 117-128, doi:10.1083/jcb.200706196 (2007).

17 Montaville, P. *et al.* Spire and Formin 2 synergize and antagonize in regulating actin assembly in meiosis by a ping-pong mechanism. *PLoS Biol* **12**, e1001795, doi:10.1371/journal.pbio.1001795 (2014).

18 Block, J. *et al.* FMNL2 drives actin-based protrusion and migration downstream of Cdc42. *Curr Biol* **22**, 1005-1012, doi:10.1016/j.cub.2012.03.064 (2012).

19 Campellone, K. G. & Welch, M. D. A nucleator arms race: cellular control of actin assembly. *Nat Rev Mol Cell Biol* **11**, 237-251, doi:10.1038/nrm2867 (2010).

20 Brandt, D. T. *et al.* Dia1 and IQGAP1 interact in cell migration and phagocytic cup formation. *J Cell Biol* **178**, 193-200, doi:10.1083/jcb.200612071 (2007).

21 Foroutannejad, S., Rohner, N., Reimer, M., Kwon, G. & Schober, J. M. A novel role for IQGAP1 protein in cell motility through cell retraction. *Biochem Biophys Res Commun* **448**, 39-44, doi:10.1016/j.bbrc.2014.04.038 (2014).

22 Gorman, J. A. *et al.* The cytoskeletal adaptor protein IQGAP1 regulates TCR-mediated signaling and filamentous actin dynamics. *J Immunol* **188**, 6135-6144, doi:10.4049/jimmunol.1103487 (2012).
23 Wagner, A. R., Luan, Q., Liu, S. L. & Nolen, B. J. Dip1 defines a class of Arp2/3 complex activators that function without preformed actin filaments. *Curr Biol* **23**, 1990-1998, doi:10.1016/j.cub.2013.08.029 (2013).
24 Balzer, C. J., Wagner, A. R., Helgeson, L. A. & Nolen, B. J. Dip1 Co-opts Features of Branching Nucleation to Create Linear Actin Filaments that Activate WASP-Bound Arp2/3 Complex. *Curr Biol* **28**, 3886-3891 e3884, doi:10.1016/j.cub.2018.10.045 (2018).
25 Balzer, C. J., Wagner, A. R., Helgeson, L. A. & Nolen, B. J. Single-Turnover Activation of Arp2/3 Complex by Dip1 May Balance Nucleation of Linear versus Branched Actin Filaments. *Curr Biol* **29**, 3331-3338 e3337, doi:10.1016/j.cub.2019.08.023 (2019).
26 Eisenmann, K. M. *et al.* Dia-interacting protein modulates formin-mediated actin assembly at the cell cortex. *Curr Biol* **17**, 579-591, doi:10.1016/j.cub.2007.03.024 (2007).
27 Satoh, S. & Tominaga, T. mDia-interacting protein acts downstream of Rho-mDia and modifies Src activation and stress fiber formation. *J Biol Chem* **276**, 39290-39294, doi:10.1074/jbc.M107026200 (2001).
28 Higashi, T. *et al.* Flightless-I (Fli-I) regulates the actin assembly activity of diaphanous-related formins (DRFs) Daam1 and mDia1 in cooperation with active Rho GTPase. *J Biol Chem* **285**, 16231-16238, doi:10.1074/jbc.M109.079236 (2010).
29 Dephoure, N. *et al.* A quantitative atlas of mitotic phosphorylation. *Proc Natl Acad Sci U S A* **105**, 10762-10767, doi:10.1073/pnas.0805139105 (2008).
30 Olsen, J. V. *et al.* Quantitative phosphoproteomics reveals widespread full phosphorylation site occupancy during mitosis. *Sci Signal* **3**, ra3, doi:10.1126/scisignal.2000475 (2010).
31 Bekker-Jensen, D. B. *et al.* An Optimized Shotgun Strategy for the Rapid Generation of Comprehensive Human Proteomes. *Cell Syst* **4**, 587-599 e584, doi:10.1016/j.cels.2017.05.009 (2017).
32 Charras, G. T., Hu, C. K., Coughlin, M. & Mitchison, T. J. Reassembly of contractile actin cortex in cell blebs. *J Cell Biol* **175**, 477-490 (2006).
33 Clark, A. G., Dierkes, K. & Paluch, E. K. Monitoring actin cortex thickness in live cells. *Biophys J* **105**, 570-580, doi:10.1016/j.bpj.2013.05.057 (2013).
34 Biro, M. *et al.* Cell cortex composition and homeostasis resolved by integrating proteomics and quantitative imaging. *Cytoskeleton (Hoboken)* **70**, 741-754, doi:10.1002/cm.21142 (2013).
35 Vargas-Pinto, R., Gong, H., Vahabikashi, A. & Johnson, M. The effect of the endothelial cell cortex on atomic force microscopy measurements. *Biophys J* **105**, 300-309, doi:10.1016/j.bpj.2013.05.034 (2013).
36 Bergert, M., Chandradoss, S. D., Desai, R. A. & Paluch, E. Cell mechanics control rapid transitions between blebs and lamellipodia during migration. *Proc Natl Acad Sci U S A* **109**, 14434-14439, doi:10.1073/pnas.1207968109 (2012).
37 Toyoda, Y. *et al.* Genome-scale single-cell mechanical phenotyping reveals disease-related genes involved in mitotic rounding. *Nat Commun* **8**, 1266, doi:10.1038/s41467-017-01147-6 (2017).
38 Sullivan-Brown, J. L. *et al.* Identifying Regulators of Morphogenesis Common to Vertebrate Neural Tube Closure and Caenorhabditis elegans Gastrulation. *Genetics* **202**, 123-139, doi:10.1534/genetics.115.183137 (2016).
39 Sokol, S. Y., Li, Z. & Sacks, D. B. The effect of IQGAP1 on Xenopus embryonic ectoderm requires Cdc42. *J Biol Chem* **276**, 48425-48430, doi:10.1074/jbc.M107975200 (2001).
40 Higashi, T., Stephenson, R. E. & Miller, A. L. Comprehensive analysis of formin localization in Xenopus epithelial cells. *Mol Biol Cell* **30**, 82-95, doi:10.1091/mbc.E18-02-0133 (2019).

41 Jones, E. A. & Woodland, H. R. Development of the ectoderm in Xenopus: tissue specification and the role of cell association and division. *Cell* **44**, 345-355 (1986).
42 Jurgenson, C. T. & Pollard, T. D. Crystals of the Arp2/3 complex in two new space groups with structural information about actin-related protein 2 and potential WASP binding sites. *Acta Crystallogr F Struct Biol Commun* **71**, 1161-1168, doi:10.1107/S2053230X15013515 (2015).
43 Luan, Q., Liu, S. L., Helgeson, L. A. & Nolen, B. J. Structure of the nucleation-promoting factor SPIN90 bound to the actin filament nucleator Arp2/3 complex. *EMBO J*, doi:10.15252/embj.2018100005 (2018).
44 Cao, L. *et al.* Modulation of formin processivity by profilin and mechanical tension. *Elife* **7**, doi:10.7554/eLife.34176 (2018).
45 Rotty, J. D. & Bear, J. E. Competition and collaboration between different actin assembly pathways allows for homeostatic control of the actin cytoskeleton. *Bioarchitecture* **5**, 27-34, doi:10.1080/19490992.2015.1090670 (2014).
46 Suarez, C. *et al.* Profilin regulates F-actin network homeostasis by favoring formin over Arp2/3 complex. *Dev Cell* **32**, 43-53, doi:10.1016/j.devcel.2014.10.027 (2015).
47 Bombardier, J. P. *et al.* Single-molecule visualization of a formin-capping protein 'decision complex' at the actin filament barbed end. *Nat Commun* **6**, 8707, doi:10.1038/ncomms9707 (2015).
48 Breitsprecher, D. *et al.* Rocket launcher mechanism of collaborative actin assembly defined by single-molecule imaging. *Science* **336**, 1164-1168, doi:10.1126/science.1218062 (2012).
49 Funk, J. *et al.* Profilin and formin constitute a pacemaker system for robust actin filament growth. *Elife* **8**, doi:10.7554/eLife.50963 (2019).

Acknowledgements
This article is dedicated to the memory of Art Alberts who passed away during completion of this study. The authors thank present and past members of the Charras, Romet/Jegou, Paluch, and Roux labs for support and discussions over the course of the project. The authors thank Alexis Gautreau and Alpha Yap for critical reading of the draft manuscript. AY, MV, PC, and MB were supported by HFSP Young Investigator grants to GC, EP, GR, and PPR (RGY66/2013). PC and EP acknowledge the support of the Medical Research Council UK (MRC programme award MC_UU_12018/5). EF was funded by a European Research Council consolidator grant to GC (CoG-647186). EB was supported by BBSRC grant (BB/R00627) to GC and RM. LC was supported by a grant from Fondation pour la Recherche Médicale (DEI 20151234415) to GRL. JM was supported by a grant from the Agence Nationale de la Recherche to AB and GRL (ANR grant Conformin). AJ was supported by a European Research Council starting grant (StG-679116). AFM equipment was funded by a BBSRC Alert16 grant to GC (BB/R000042). AM and GL were supported by an Operating grant from the Canadian Institute of Health Research to P.P.R. (MOP‑142374). PPR is supported by a FRQS Senior investigator career award. The authors also wish to thank Henry Higgs, Robert Grosse, Brad Nolen, David Sacks, Robert Tombes, and Orion Weiner for sharing reagents.

Author contributions
GC, GRL, AJ, AY, LC, and MV designed the experiments. AY carried out all electron microscopy on cells, long term microscopy, and bleb size characterization. MV carried out all laser ablation, AFM and fluorescence quantification experiments. LC, GRL, AJ carried out in vitro experiments. PC did all measurements of cortex thickness and F-actin density. MS designed the software for analysis of SEM images. GL, AM, and PPR performed all proteomic and qPCR experiments and analyzed data. AY and EF did all Western blots. GC generated plasmid constructs and cell lines, and carried out immunostainings. JM and AB carried out the molecular-scale electron microscopy and generated the complex structures. MB contributed live imaging constructs and some imaging experiments. AA provided plasmid constructs. EB and RM contributed Xenopus experiments. EP provided conceptual advice. GC and GRL wrote the manuscript. All authors discussed the results and the manuscript.

Conflict Financial Interests
The authors declare no competing financial interests

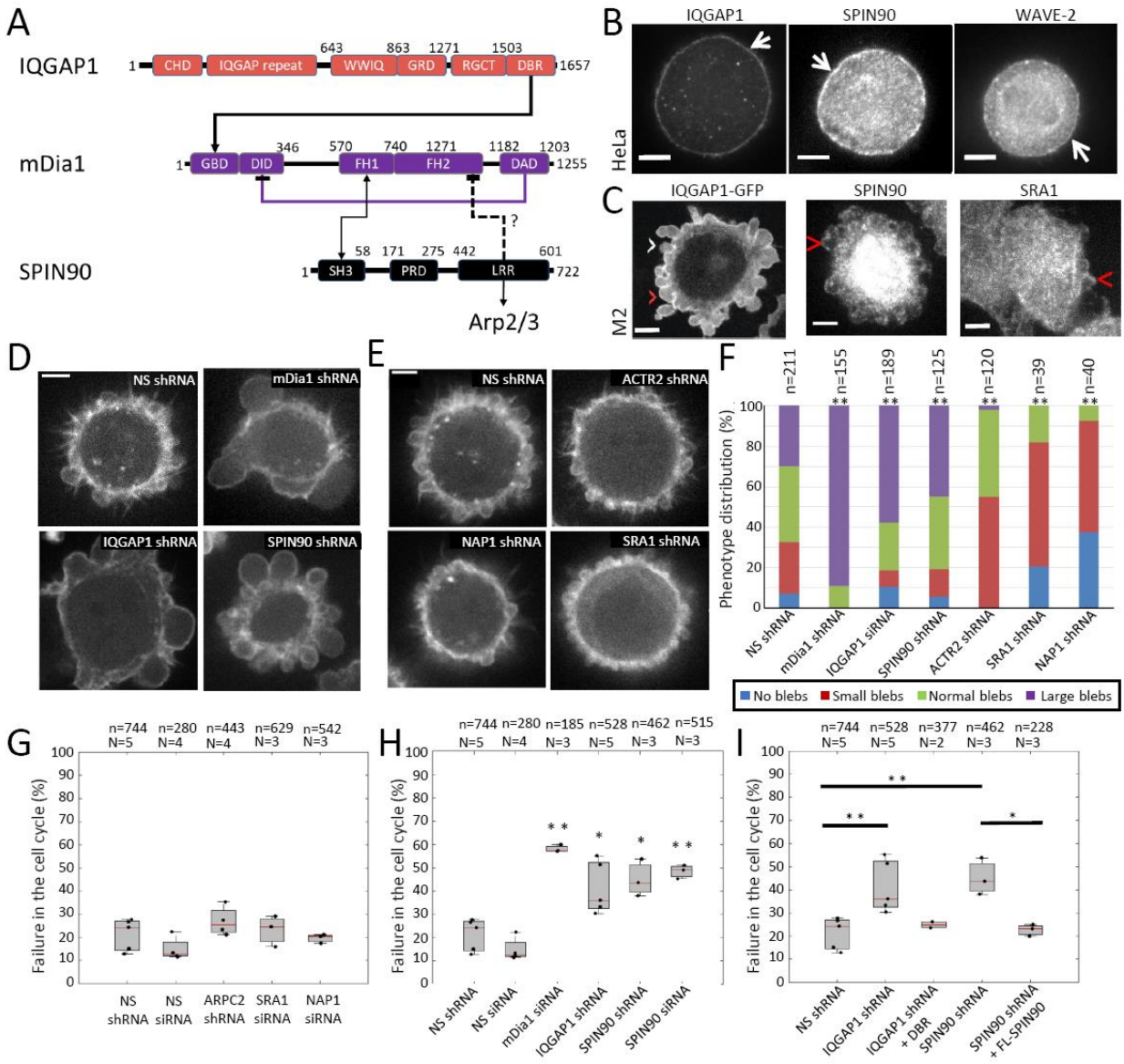

Figure 1: Several Nucleation Promoting Factors are present in the actin cortex. A. Domain structure of IQGAP1, mDia1, and SPIN90. Amino-acid position is given from the N terminus. Known protein interactors are displayed under each domain. Known positive and inhibitory interactions between IQGAP1, mDia1, and SPIN90 are indicated. **B. L**ocalization of NPFs in metaphase HeLa cells detected by immunofluorescence. Arrows indicate cortical localization. Scale bars=5µm. **C.** Localization of NPFs in M2 blebbing melanoma cells. IQGAP1 localization was obtained through transient transfection with IQGAP1-GFP. The SRA1 subunit of the WAVE complex and SPIN90 were detected by immunofluorescence. White arrowheads indicate expanding blebs and red arrowheads retracting ones. Scale bars=5µm. (**D-E).** Live confocal microscopy images of M2 blebbing melanoma cells stably expressing LifeAct-Ruby and stably transduced with shRNA targeting (**D**) mDia1, IQGAP1, SPIN90 and (**E**) ACTR2 (the Arp2 subunit of the Arp2/3 complex), NAP1, and SRA1 as well as Non-Silencing shRNA. Scale bars=5 µm. **F.** Distribution of bleb sizes in M2 cells stably expressing Non-Silencing shRNA, mDia1 shRNA, ACTR2 shRNA, IQGAP1 shRNA, SPIN90 shRNA, SRA1 shRNA, and NAP1 shRNA. Representative cells are displayed in D-E. . The total number (n) of cells examined in three independent experiments is indicated above each column. Comparison to Non-Silencing shRNA with Chi-squared test (**Supplementary Table 4**): mDia1: p=3 10^{-56}; IQGAP1: p=3 10^{-18}; SPIN90: p=6 10^{-4}; ACTR2: p=2 10^{-17}; SRA1: p=1 10^{-9}; NAP1: p=4 10^{-18} (**, p<0.01)**.** Experiments in **B-E** were repeated three times

independently with similar results. **(G-I)** Percentage of HeLa cells failing to progress through the cell cycle. Statistics are derived from the total number (n, indicated above each box) of cells examined in independent experiments (N, indicated above each box). The average for each independent experiment is shown by a black dot. The distributions' medians, first and third quartiles and ranges are represented by the central red bars, bounding boxes and whiskers, respectively. Targeting si/shRNAs were compared statistically to Non-silencing si/shRNA with Welch's two-sided t-test. **G.** Cells transfected with ARPC2 shRNA, SRA1 siRNA, and NAP1 siRNA. ARPC2: p=0.24; SRA1: p=0.14; NAP1: p=0.15. **H.** Cells transfected with mDia1 siRNA, IQGAP1 shRNA, and SPIN90 si/shRNA (*, p<0.05; **, p<0.01). mDia1: p=9 10^{-5}; IQGAP1: p=0.026; SPIN90 siRNA: p=1 10^{-4}; SPIN90 shRNA: p=0.01. **I.** Rescue experiments for SPIN90 shRNA and IQGAP1 shRNA. Statistical comparison to Non-Silencing shRNA: IQGAP1 shRNA+DBR: p=0.33; SPIN90 shRNA + FL: p=0.7. Statistical source data can be found at Source data figure 1.

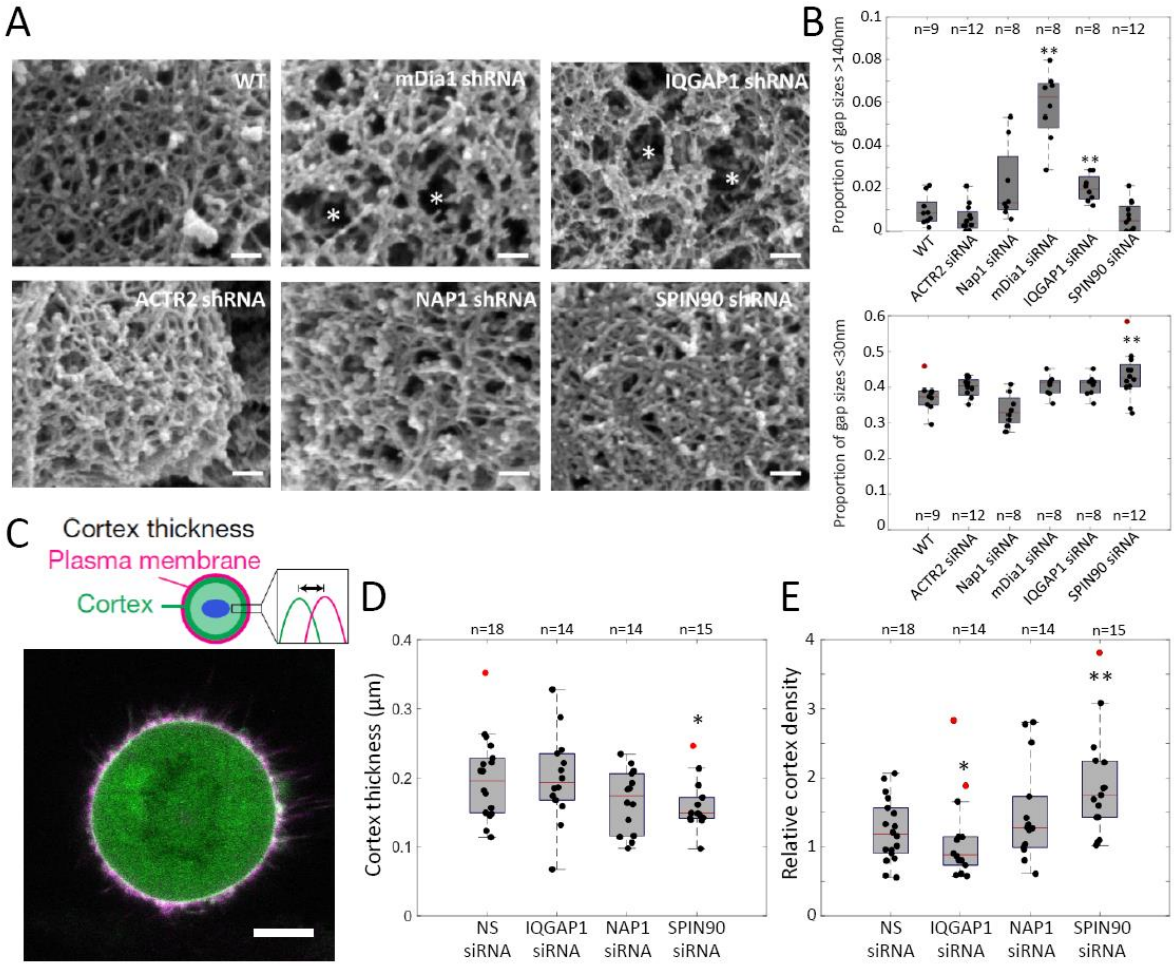

Figure 2: SPIN90 controls cortex molecular-scale organization. A. Representative scanning electron micrographs of the actin cortex at the surface of a bleb in detergent-extracted M2 cells stably expressing non-silencing shRNA or shRNA targeting nucleators or NPFs. Asterisks highlight large gaps in the cortex. Scale bars = 100 nm. **B.** Frequency distribution of gap diameters within the cortical mesh of blebs in M2 cells. Comparison to WT with two-sided Wilcoxon's rank test for small mesh sizes (bottom, <30nm, **<p=0.01): Arp2: p=0.03; Nap1: p=0.12; mDia1: p=0.08; IQGAP1: p=0.04; SPIN90:

p=0.01. For large mesh sizes (top, >140nm, **<p=0.01): Arp2: p=0.24; Nap1: p=0.09; mDia1: p=0.01; IQGAP1: p=0.01; SPIN90: p=0.81. The full distributions are presented in **Supplementary Figure 3**. **C.** Top: Schematic representation of the measurement: cortex thickness and density are extracted from the fluorescence profiles of mCherry-CAAX (plasma membrane) and GFP-actin (cortex) in prometaphase HeLa cells[33]. Bottom: Representative confocal image of a prometaphase HeLa cell expressing GFP-actin (green) and mCherry-CAAX (magenta). Scale bar=10 µm. **D.** Cortex thickness for prometaphase HeLa cells transfected with non-silencing siRNA or siRNA targeting IQGAP1, NAP1, SPIN90. **E.** Cortex density for prometaphase HeLa cells transfected with non-silencing siRNA or siRNA targeting IQGAP1, NAP1, SPIN90. **(D-E)** *p<0.05 and **p<0.01 compared to the appropriate control with two-sided Welch's t-test. Cortex thickness: IQGAP1: p=0.59; Nap1: p=0.2; SPIN90: p=0.02. Cortex density: IQGAP1: p=0.03; Nap1: p=0.26; SPIN90: p=0.007. (**B**, **D-E**) The distributions' medians, first and third quartiles and ranges are represented by the central red bars, bounding boxes and whiskers, respectively. Statistics are derived from the total number of cells (n, indicated above or below each box) examined in three independent experiments. Statistical outliers are indicated by red dots. SEM data in **A** are representative of two independent experiments. Cortical thickness and density measurements are derived from data gathered from three independent experiments. Statistical source data can be found at Source data figure 2.

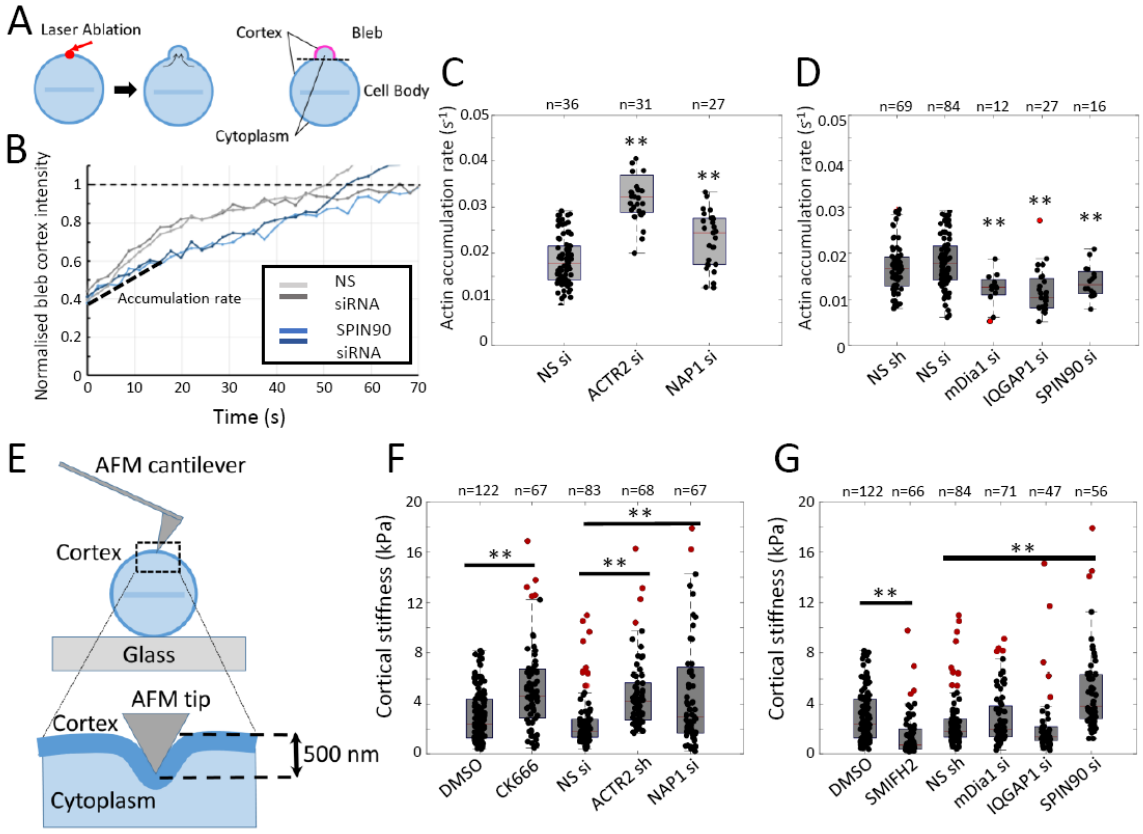

Figure 3: SPIN90 controls regrowth kinetics and mechanics. A. Illustration of the procedure to induce single blebs by laser ablation of the cortex in metaphase HeLa cells (red arrow)[34]. Right: cells are segmented into cytoplasm, cell body cortex, and bleb cortex to allow measurement of fluorescence intensity in these regions over time (**Extended Data Fig. 2A-C**). **B.** Representative actin regrowth

curves in blebs induced by laser ablation in metaphase HeLa cells expressing LifeAct-Ruby transfected with Non-silencing siRNA (grey) or SPIN90 siRNA (blue). The mean actin fluorescence intensity at the bleb cortex was normalized to that in the cell body cortex (dashed horizontal line). Initial regrowth rates after ablation are linear with time (initial accumulation rate, dashed line). t = 0 s, ablation onset. Experiments were repeated three times independently with similar results. The number of independent cells examined is n=36 for Non-silencing siRNA and n=16 cells for SPIN90 siRNA. **C-D.** Actin cortex accumulation rate in cells transfected with non-silencing siRNA/shRNA (NS si/ Ns sh) or siRNA/shRNA targeting nucleators and NPFs. Statistical comparison to the appropriate control using two-sided Student's t-test: ACTR2: $p=9\ 10^{-20}$; Nap1: p=0.002; mDia1: p=0.001; IQGAP1: $p=2\ 10^{-5}$; SPIN90: p=0.001. **E.** Principle of Atomic Force Microscopy cortex stiffness measurement. The pyramidal AFM tip indents the cell cortex (dark blue) to a depth of 500nm. Controls are presented in **Extended Data Fig. 2D-E**. **F.** Cortical stiffness for control cells (DMSO, NS siRNA) and cells treated with the Arp3 inhibitor CK666 or expressing si/shRNAs targeting NAP1 and ACTR2. **G.** Cortical stiffness for control cells (DMSO, NS shRNA) and cells treated with the formin inhibitor SMIFH2 or expressing si/shRNAs targeting mDia1, IQGAP1, and SPIN90. Statistical comparison to the appropriate control using two-sided Student's t-test: ACTR2: $p=2\ 10^{-18}$; Nap1: $p=2\ 10^{-10}$; CK666: $2\ 10^{-6}$; mDia1: p=0.06; IQGAP1: p=0.03; SPIN90: p=0.0002; SMIFH2: $p=2\ 10^{-11}$. **p < 0.01. (**C-D**, **F-G**) The distributions' medians, first and third quartiles and ranges are represented by the central red bars, bounding boxes and whiskers, respectively. The number of independent cellular measurements (n, indicated above each box) is pooled from three independent experiments. Statistical outliers are indicated by red dots. Statistical source data can be found at Source data figure 3.

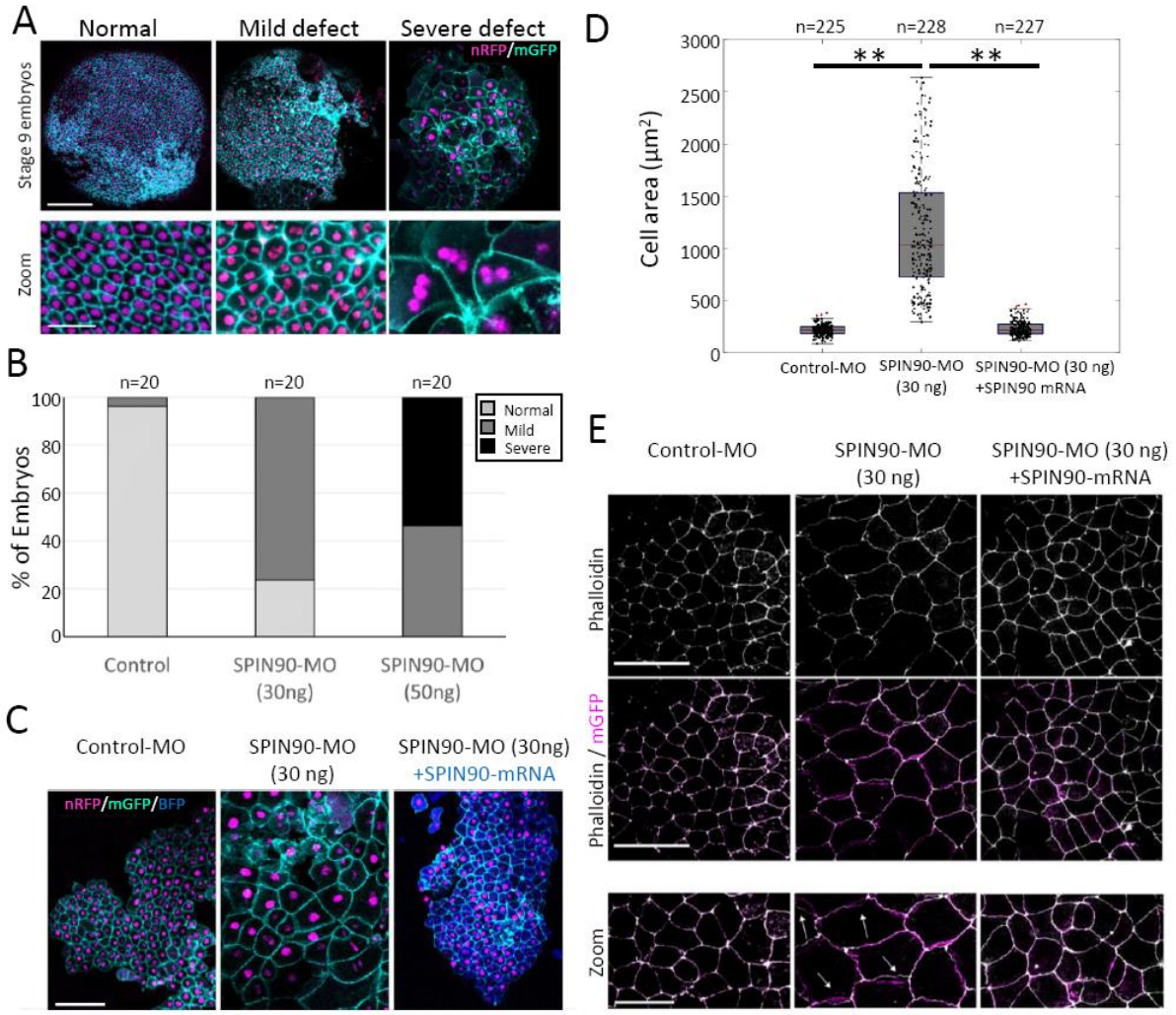

Figure 4. SPIN90 is necessary for correct development of *Xenopus* blastulae. A. Stage 9 *Xenopus* embryos (St9) injected with Control-MO or SPIN90-MO along with nuclear targeted RFP (nRFP) and membrane targeted GFP (mGFP). Images are representative of normal ectoderm (left) and ectoderm with mild (middle) or severe (right) defects in cell numbers and cell size. Scale bars: top row: 150 µm; bottom row: 50 µm. **B.** Proportion of embryos with normal ectoderm (light grey) and mild (dark grey) or severe (black) defects for different morpholino injections. Experiments were repeated four times independently with similar results. Knock-down validation is presented in **Supplementary Figure 5**. **C.** Stage 9 *Xenopus* embryos (St9) co-injected with: Control-MO (30ng), SPIN90-MO (30ng), or SPIN90-MO (30ng) plus full-length mouse SPIN90-BFP, along with nuclear targeted RFP and membrane targeted GFP. The efficiency of the rescue was 70% with just 10% of the embryos displaying morphant phenotype, compared to ~80% displayed by SPIN90-MO treated embryos. Images are representative of three independent experiments with similar results. Scale bar: 100 µm. **D.** Cell area for stage 9 *Xenopus* embryos injected with Control-MO (30ng), SPIN90-MO (30ng), or SPIN90 (30ng) + mouse SPIN90 mRNA. The distributions' medians, first and third quartiles and ranges are represented by the central red bars, bounding boxes and whiskers, respectively. The number of independent cellular measurements (n, indicated above each box) was pooled from three independent experiments. Statistical outliers are indicated by red dots. Statistical comparison with Welch's two-sided t-test: Control-MO vs SPIN90-MO: $p=3\ 10^{-131}$; SPIN90-MO vs rescue: $p=5\ 10^{-122}$; Control-MO vs rescue: p=0.20. **p < 0.01. **E.** Stage 9 *Xenopus* embryos (St9) co-injected with Control-MO, SPIN90-MO, or SPIN90-MO plus full-length mouse SPIN90-BFP mRNA, along with membrane targeted GFP. Top panels display phalloidin staining (white), central panels show the overlap with membrane targeted GFP (magenta), and lower panels show a zoom of the middle panels. In some SPIN90-MO treated cells,

actin is no longer colocalized with cell membranes, white arrows. Scale bars: Top and middle panels: 100 µm. Bottom panel: 50 µm. Images are representative examples of three independent experiments with similar results. Statistical source data can be found at Source data figure 4.

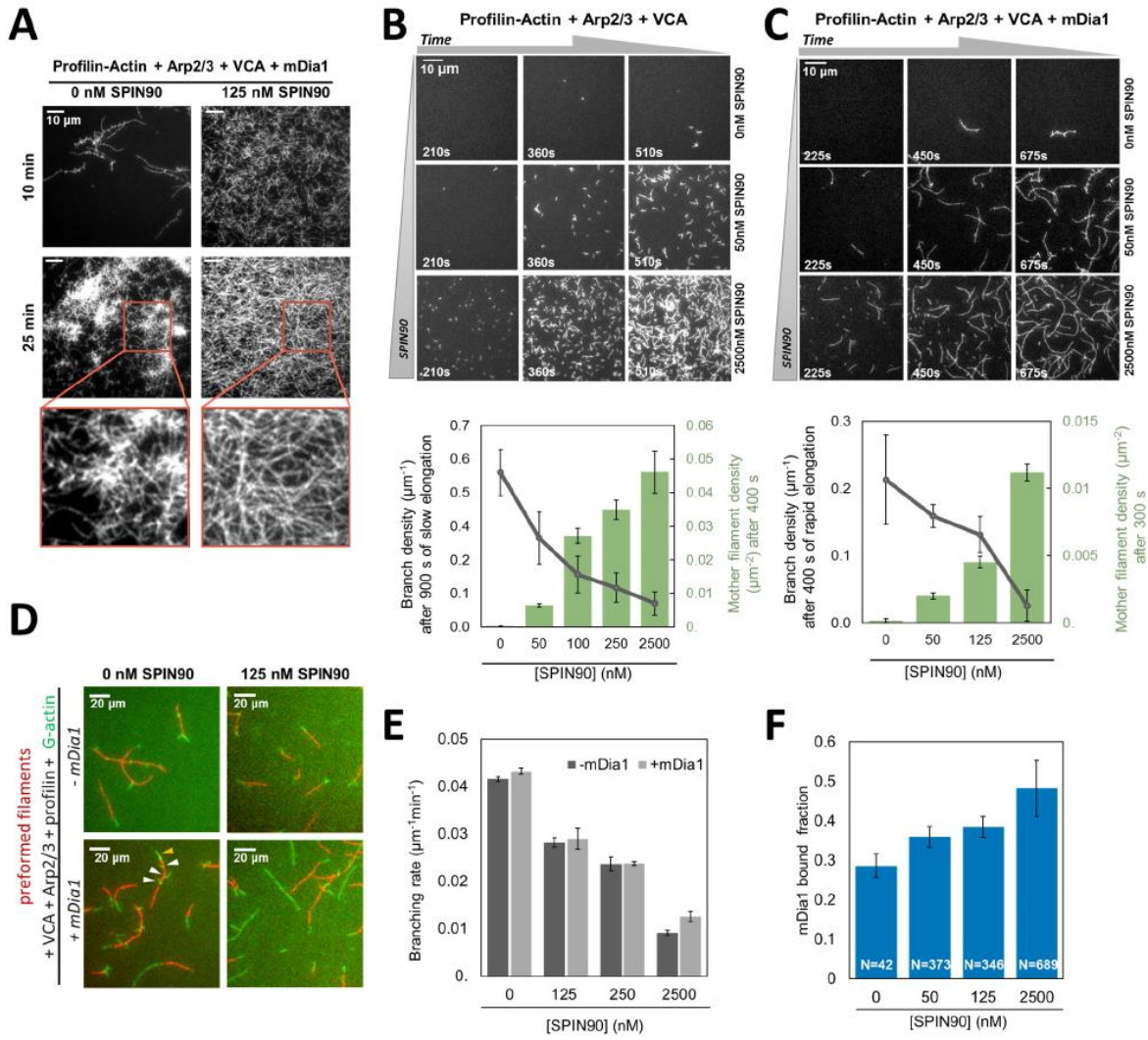

Figure 5. SPIN90 activates Arp2/3 to nucleate filaments and favours mDia1-induced elongation. A. TIRF images of 0.5µM actin (15% Alexa488 labeled) polymerizing in the presence of 0.5 µM profilin, 25 nM Arp2/3 complex, 50 nM VCA, 0.2 nM mDia1, with (right) and without (left) 125 nM SPIN90. **B-C.** TIRF images of the same protein solution as in A, without mDia1 (**B**) and with 0.4 nM mDia1 (**C**), and with various concentrations of SPIN90 (indicated on the right side of each row). Plots: nucleation (green bars) is quantified by counting the number of mother filaments over 56063 µm^2 after 400 seconds (**B**) or 300 seconds (**C**), and (± 95 % confidence interval.). The branch density (gray points) is quantified as the number of branches per micrometer of mother filament (± 95 % confidence interval, counted on n=20 mother filaments for each condition gathered in one experiment, except n=10 for 0 nM SPIN90 in **C**). Branches were counted after mother filaments had elongated for 900 s, typically becoming 5.5µm long (**B**) or after mother filaments had elongated with mDia1 for 400s, typically becoming 18µm long (**C**). **D.** TIRF microscopy images of preformed actin filaments (15% Alexa568-

labeled, red) mixed with the same protein solution as in **A**, with or without 0.2 nM mDia1, with or without 125 nM SPIN90. The result is plotted in **E**: the branching rate (± std. error) is determined from the number of branches appearing on the preformed mother filaments over time (**Supplementary Figure 7**), as a function of SPIN90 concentration, in the absence (dark grey bars) or presence (light grey bars) of 0.2nM mDia1. **F.** Fraction of rapidly growing barbed ends (i.e. bearing a formin), observed after 400s in the experiment shown in (**C**). Error bars represent 95% confidence intervals. The number of filaments (N) is indicated below each bar. (**D-F**) Measurements were gathered from two independent experiments. (B-F) were repeated twice, and (A) three times, independently, with similar results. Statistical source data can be found at Source data figure 5.

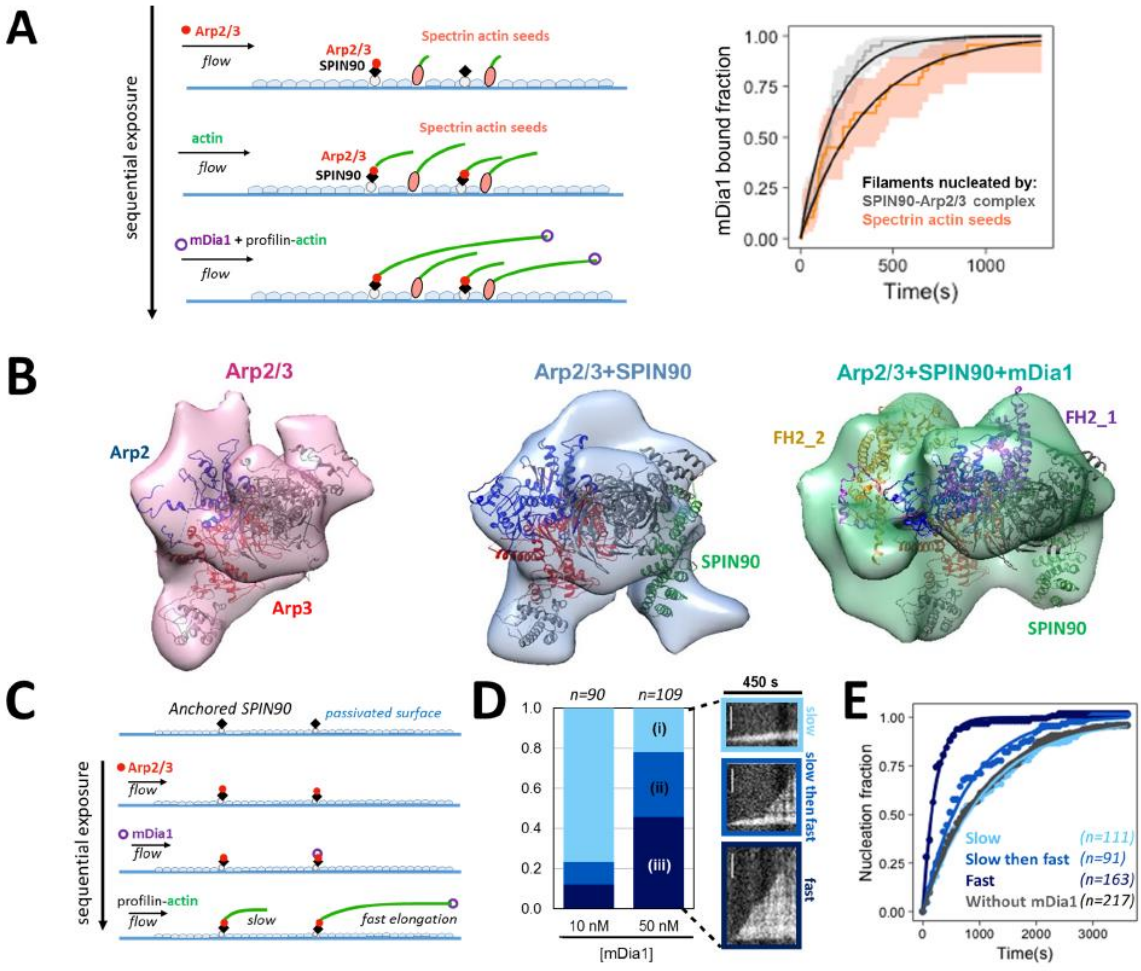

Figure 6. mDia1 binds preferentially to SPIN90-Arp2/3 filaments and forms a ternary complex with SPIN90-Arp2/3 to generate fast-elongating filaments. A. In a microfluidics experiment, filaments were nucleated by surface-anchored spectrin-actin seeds or SPIN90-Arp2/3 complexes, and identified as such (**Extended Data Fig. 9A-B**) before flowing in a solution containing 0.5 µM G-actin (15% Alexa488 labeled), 3.5 µM profilin and 0.4 nM mDia1. Acceleration of elongation indicated the binding of mDia1. Plot: measured mDia1-elongating filament fractions versus time and exponential fits (black lines), for filaments nucleated by spectrin-actin seeds (pink, n=39 filaments, $k_{on}=2.8x10^{-3} \pm 1.1x10^{-5}$ s^{-1}) and by SPIN90-Arp2/3 (gray, n=40 filaments, $k_{on}=5.5x10^{-3} \pm 3.5x10^{-5}$ s^{-1}). Two-sided log-rank test:

p=0.01. Shaded regions, 95% confidence intervals. **B.** 3D structures of protein complexes reconstructed from EM negative stains, at 27Å resolution, from Arp2/3 incubated with mDia1 (left), SPIN90 (middle) or both (right). EM densities were fitted using UCSF Chimera with crystal structures of Arp2/3 (PDB : 4xf2) (left) or Arp2/3-SPIN90 complex (PDB : 6dec) (middle), or an atomic model of an mDia1 FH2 dimer (PDB : 1y64) bound to the Arp2/3-SPIN90 complex (PDB : 6dec) (right). Further information: **Extended Data Fig. 7-8**. **C.** Microfluidics experiment where a SPIN90-decorated surface is sequentially exposed to Arp2/3 then mDia1, before flowing in profilin-actin. Filaments are observed with their pointed ends attached to the surface and their barbed ends growing either slowly (bare barbed ends) or rapidly (mDia1-bearing barbed ends). **D**. Proportion of filaments elongating slow (i, light blue), slow-then-fast (ii, blue) and fast (iii, dark blue) for different mDia1 concentrations, illustrated by representative kymographs. The SPIN90-decorated surface was exposed to 40 nM Arp2/3 (for 120s), followed by 10 or 50 nM mDia1 (30s), then buffer (120s), and finally filaments were observed in the presence of 0.5 µM actin and 0.5 µM profilin. Scale bar=5µm **E.** Nucleation of the three filament populations observed in (**D**) with 50 nM mDia1, compared to the nucleation of filaments in a chamber region unexposed to mDia1 (grey) (**Extended Data Fig. 9C**). Exponential fits (lines) yield nucleation rates of 8.8×10^{-4} s^{-1} for (i), 1.2×10^{-3} s^{-1} for (ii) (p=0.1, two-sided log-rank test) and 4.6×10^{-3} s^{-1} for (iii) ($p=2 \times 10^{-16}$, two-sided log-rank test). n in D and E indicates the total number of filaments analyzed in one experiment. Experiments in (A) were repeated twice, and in (C-E) three times, independently, with similar results. Statistical source data can be found at Source data figure 6.

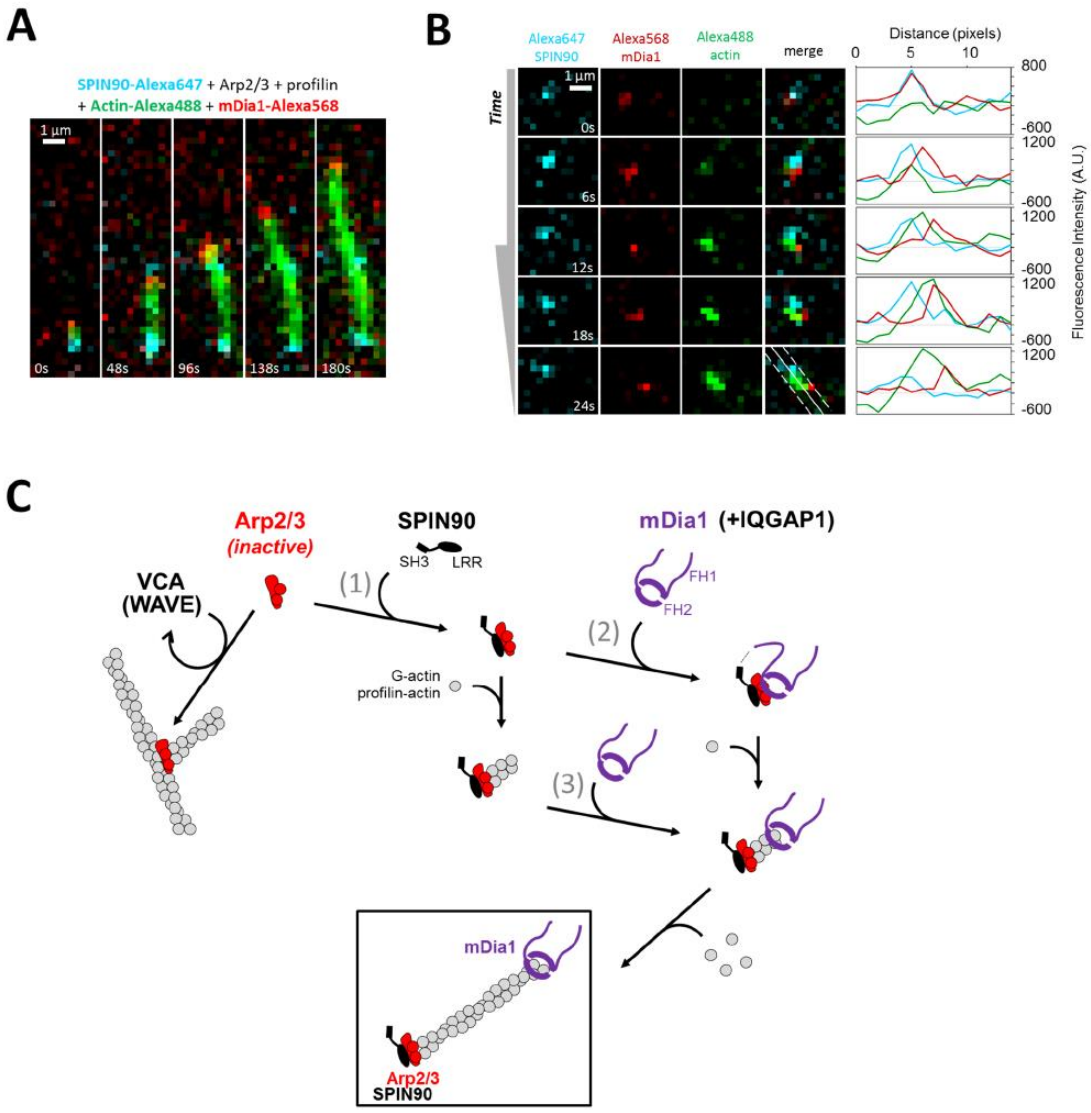

Figure 7. Illustration of the interplay between SPIN90, mDia1, and Arp2/3 at the molecular level. A. TIRF microscopy image sequence of an elongating filament in a solution of 0.4 µM actin (15% Alexa488 labelled, green), 0.6 µM profilin, 2 nM SPIN90-Alexa647 (cyan), 120 nM Arp2/3 and 1 nM mDia1-SNAP549 (red). **B.** TIRF microscopy image sequence of a filament nucleated from SPIN90-Alexa647 (cyan), Arp2/3 and mDia1-SNAP549 (red). Same conditions as in (**A**). Intensity plots were taken along the white solid line shown in the bottom right image, over a 3-pixel width (dashed lines). (**A,B**) Scale bars=1µm. Experiments were repeated twice independently with similar results. **C**. Interplay at the molecular level. SPIN90 activates the Arp2/3 complex (reaction 1) to nucleate linear filaments, in competition with Arp2/3 branching (left) following activation by the WAVE complex (not sketched) and binding to the sides of existing filaments. SPIN90 remains bound to the activated Arp2/3 complex at the pointed end of the nucleated filament. Formin mDia1, maintained in an active conformation by IQGAP1 (not sketched), can bind to the filament barbed end and accelerate its elongation using profilin-actin. Barbed ends nucleated by SPIN90-Arp2/3 are particularly prone to binding mDia1 (reaction 3). Formin mDia1 can also bind to the SPIN90-Arp2/3 complex, forming a ternary complex (reaction 2), which efficiently nucleates rapidly growing filaments. Both routes lead to the formation of filaments with mDia1 at their barbed ends and SPIN90-Arp2/3 at their pointed ends. Note that active WAVE complex and active mDia1 are likely anchored to the plasma membrane.